Inorganic Chemistry

ARTICLE

pubs.acs.org/IC

Photochemical Two-Electron Reduction of a Dinuclear Ruthenium Complex Containing a Bent Tetraazatetrapyridopentacene Bridging Ligand: Pushing Up the LUMO for Storing More Energy

Shreeyukta Singh,[†] Norma R. de Tacconi,[†] N.R.G. Diaz,[†] Reynaldo O. Lezna,*[,‡] Jackeline Muñoz Zuñiga,[‡] Kenneth Abayan,[†] and Frederick M. MacDonnell*[,†]

[†]Department of Chemistry and Biochemistry, The University of Texas at Arlington, Arlington, Texas 76019-0065, United States

[‡]Instituto de Investigaciones Fisicoquímicas Teóricas y Aplicadas (INIFTA, UNLP, CCT La Plata-CONICET), Sucursal 4, C.C. 16, (B1906ZAA) La Plata, Argentina

ABSTRACT: The synthesis and characterization of a ditopic bridging ligand, 9,12,21,22-tetraazatetrapyrido[3,2-*a*:2′,3′-*c*:3″2″-*m*:2‴,3‴-*o*]pentaphene (tatppα) and its dinuclear ruthenium complex, $[(phen)_2Ru(tatppα)Ru(phen)_2][PF_6]_4$ ($\mathbf{1}^{4+}$), are described. The tatppα ligand is structurally very similar to 9,10,20,33-tetraazatetrapyrido[3,2-*a*:2′,3′-*c*:3″,2″-*l*:2‴,3‴-*n*]pentacene (tatpp*β*), except that, instead of a linear tetraazapentacene backbone, tatppα has an ortho (or α) substitution pattern about the central benzene ring, leading to a 120° bend. Complex $\mathbf{1}^{4+}$ shows tatppα-based reductions at −0.73 and −1.14 V vs Ag/AgCl/saturated KCl and has an absorption spectrum showing the typical Ru^{II} d$\pi \rightarrow$ phen-like π^* metal-to-ligand charge-transfer transition centered at ∼450 nm. In acetonitrile, visible-light irradiation of $\mathbf{1}^{4+}$ in the presence of triethylamine leads to two sequential changes in the absorption spectra, which are assigned to the formation of the one- and two-electron-reduced species, with the electrons stored on the tatppα ligand. These assignments were made by comparison of the spectral changes observed in $\mathbf{1}^{4+}$ upon stoichiometric chemical reduction with cobaltocene and by spectroelectrochemical analysis. Significantly, DFT calculations are very predictive of the optical and reductive behavior of the tatppα complex relative to the tatpp*β* complexes and show that modeling is a useful tool for ligand design. The chemical reactivity and differential reflectance spectroelectrochemical data reveal that the reductions are accompanied by radical dimerization of the tatppα ligand to species such as σ-$\{\mathbf{1}\}_2^{6+}$, which is only slowly reversible upon exposure to air and may limit the complexe's $\mathbf{1}^{4+}$ utility for driving photochemical H_2 production.

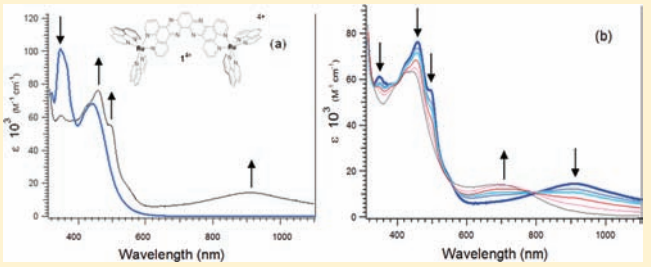

INTRODUCTION

Ruthenium polypyridyl complexes continue to draw attention as potential chromophores for artificial photosynthetic assemblies, with the goal of producing solar fuels from water and CO_2.[1−3] The hydrogen- and oxygen-evolving reactions are central to most practical solar fuel-formation schemes, yet photosystems to drive these remain elusive.[4] These fuel-formation reactions are all multielectron processes, whereas chromophore photoexcitation is almost always a one-photon, one-electron process.[5] While it is possible to drive these reactions in one-electron steps,[6] certain efficiencies may be realized by using catalysts capable of multielectron reductions.[5] As demonstrated by the oxygen-evolving system in natural photosystems, properly designed multielectron catalysts can build up redox equivalents and then deliver them in a single step to drive a multielectron process, in this case the four-electron oxidation of water to O_2.[7,8] Similarly, enzymes that drive multielectron reductions are known; however, practical synthetic or "artificial" photochemical systems for even simple reactions such as H_2 production remain a challenge. One common problem is that the first photoreduction changes the physical properties of the initial acceptor orbital such that successive electron-transfer events are usually not favorable.[9,10]

The groups of Brewer,[11−13] Nocera,[9,14,15] and Bocarsly[16,17] have all reported on photochemically active complexes that undergo multiple photoreductive processes, some of which catalyze H_2 formation under appropriate conditions. Of these, only one complex, a Ru^{II}−Ir^{III}−Ru^{II} trimer, is reported to store the electrons in ligand-based acceptor orbitals, and in this case, the two electrons are stored on different ligands.[18] There are numerous reports of using ruthenium polypyridyl complexes as chromophores for photocatalytic H_2 formation,[19−24] normally with a hydrogen-evolving cocatalyst added to the solution or tethered directly to the ruthenium chromophore; however, the mechanism and intermediates by which H_2 is formed are not clear.

Received: March 31, 2011
Published: August 26, 2011

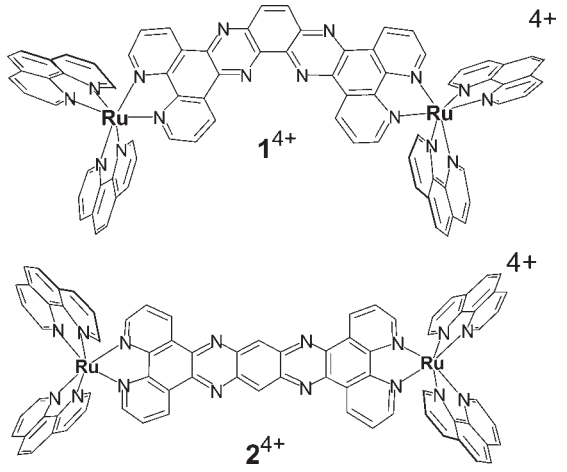

Figure 1. Structures of dinuclear ruthenium complexes $\mathbf{1}^{4+}$ and $\mathbf{2}^{4+}$ containing the tatppα and tatppβ ligands, respectively.

Our group has reported that ruthenium(II) polypyridyl complexes based on tetraazatetrapyridopentacene (tatppβ), shown in Figure 1, and structurally related acceptor ligands are capable of photodriven multielectron storage.[25,26] In complexes such as $[(phen)_2Ru(tatpp\beta)Ru(phen)_2]^{4+}$ ($\mathbf{2}^{4+}$) and $[(phen)_2Ru(tatpq)Ru(phen)_2]^{4+}$ ($\mathbf{3}^{4+}$), where tatpq is 9,11,20,22-tetraazatetrapyrido[3,2-*a*:2′,3′-*c*:3″,2″-*l*:2‴,3‴-*n*]pentacene-10,21-quinone, the photoreductions occur by stepwise one-electron processes involving the reductive quenching of the triplet metal-to-ligand charge-transfer (^{3}MLCT) state commonly formed in ruthenium(II) polypyridyl complexes. The resulting photoreduced complex stores the electron in a low-energy acceptor orbital on the tatppβ or tatpq bridging ligand, leaving the higher-energy "phenanthroline-like" acceptor orbital unoccupied and available for "reduction" upon subsequent photoexcitation into the MLCT band or the reduced complex. Reductive quenching by an external donor and electron transfer to the low-lying acceptor orbital results in anywhere from two to four electrons being stored on the bridging ligand and empties the "phen-like" orbital for subsequent photoexcitations. The unusual acceptor capabilities of tatpp and tatpq bridging ligands seem to arise from the weak electronic coupling of the low-energy central acceptor orbitals with the Ru dπ donor orbitals, such that photoexcitation does not directly populate these orbitals. We are calling this type of ligand laminate acceptor ligand to indicate the roles of two or more spatially overlapping acceptor orbitals in defining the ground- and excited-state redox and optical properties of the complexes.

The challenge with using these complexes for solar fuel production is that the stored electrons do not have sufficient energy to form H_2 upon reaction with hydrogen-evolving catalysts. Photolysis of $\mathbf{3}^{4+}$ in the presence of triethylamine, triethylammonium ion, and a hydrogen-evolving cocatalyst $[Pt(bpy)Cl_2]$ gives only two or three H_2 per $\mathbf{3}^{4+}$ per day, and complex $\mathbf{2}^{4+}$ is essentially inactive to H_2 production.[4,27] However, the design elements for photon-driven multielectron storage were elucidated. The complex should have high-energy optical acceptor orbitals and lower-lying redox orbitals, which are decoupled from the Ru dπ highest occupied molecular orbital (HOMO).

The presence of two distinct acceptor orbitals, a high-energy optical orbital, and a lower-lying redox orbital was first described for the dppz-containing complexes, $[(phen)_2Ru(dppz)]^{2+}$ and $[(bpy)_2Ru(dppz)]^{2+}$.[28−32] The optical and redox orbitals are described as being localized on the proximal (bpy-like) and distal (phenazine-like) portion of the dppz ligand, respectively. Despite similar electronic structures, photolysis of $[(phen)_2Ru(dppz)]^{2+}$ in the presence of sacrificial donors only produces the singly reduced $[(phen)_2Ru(dppz^{\bullet-})]^{+}$, revealing that if the energy of the redox orbital is too high, the complex can "self-quench".

The aim of this work was to design an acceptor ligand containing a "phen-like" optical orbital and a lower-lying redox orbital, which would retain the ability to store multiple electrons in a photochemical process, yet store these electrons at potentials that would be useful for fuel-forming reactions, i.e., H_2 formation. In this report, we describe the synthesis of a new laminate acceptor ligand, tatppα, and its dinuclear complex $[(phen)_2Ru(tatpp\alpha)Ru(phen)_2]^{4+}$ ($\mathbf{1}^{4+}$), shown in Figure 1. The optical, electrochemical, and photochemical properties of this new complex as well as an optical study of the chemically and electrochemically reduced forms of $\mathbf{1}^{4+}$ are investigated. Using a combination of voltammetry and differential reflectance measurements, we also elaborate on the multistep photochemical and electrochemical reduction mechanism and speciation of complex $\mathbf{1}^{4+}$.

EXPERIMENTAL SECTION

All of the reagents and solvents used were of reagent grade and were used as received unless otherwise noted. 1,10-Phenanthroline-5,6-dione (phendione),[33] $Ru(phen)_2Cl_2$ (phen = phenanthroline),[34] and 11-nitrodipyrido[3,2-*a*:2′,3′-*c*]phenazine (11-nitrodppz)[31,35] were synthesized based on literature procedures. Acetonitrile (Aldrich, 99.93+%, HPLC grade) was kept over molecular sieves (3 Å) and passed through a column packed with neutral chromatographic alumina just before use. Cobaltocene (Alfa Aesar) was used as received. Bu_4NPF_6 (Aldrich) was dried overnight under vacuum at 60 °C and stored under nitrogen prior to use.

NMR spectra were recorded at 25 °C on a JEOL Eclipse 500 spectrometer (^{1}H, 500.16 MHz,). Proton chemical shifts are reported in ppm, referenced to the residual proton peaks of the solvent, and quoted relative to Me_4Si. Melting points were obtained on a Mel-Temp II apparatus and were not corrected.

Redox titrations were carried out in a nitrogen atmosphere glovebox (max $[O_2]$ < 3 ppm) and used freshly prepared stock solutions of $\mathbf{1}[PF_6]_4$ (1.0×10^{-4} M) and $Co(Cp)_2$ (0.01 M), the latter as the reducing agent. Both solutions were prepared in distilled and degassed acetonitrile in the glovebox. The final concentration in the cuvette was 15 μM $\mathbf{1}[PF_6]_4$. Thus, stepwise chemically reduced species of $\mathbf{1}^{4+}$ were generated with the addition of 1 and 2 equiv of $Co(Cp)_2$, respectively, and characterized by UV−visible spectroscopy using a Hewlett-Packard diode-array spectrometer (model 8433).

Photochemical reduction was performed in a sealed photochemical cell degassed with argon gas for 10 min prior to irradiation. The cell was kept at 22 °C by immersion in a water bath, while irradiated with the full output of a 100 W tungsten halogen lamp. The photon flux was 1.12×10^6 lux, as measured by a Lutron LX101m. The progress of the photochemical reaction was monitored by recording the absorption spectra. Triethylamine (TEA) was used as a sacrificial electron donor.

Electrochemical data were obtained with a CHI620C electrochemical analyzer (CH Instruments, Austin, TX). A single-compartment, three-electrode electrochemical cell was used with either glassy carbon (1.5-mm-diameter disk) or platinum (1.0-mm-diameter disk) from Cypress Systems as the working electrode. Immediately before use, the electrode was polished to a mirror finish with wet alumina (Buehler, 0.05 μm), followed by rinsing with Millipore Milli-Q water and sonication. A platinum wire and a nonleaking Ag/AgCl/saturated KCl reference

dx.doi.org/10.1021/ic2006698 |*Inorg. Chem.* 2011, 50, 9318–9328

electrode (Cypress Systems, model EE009) were used as the counter and reference electrodes, respectively. All potentials were measured and are quoted versus a Ag/AgCl/saturated KCl reference electrode. All electrochemical data were recorded in acetonitrile with 0.1 M Bu_4NPF_6 as the supporting electrolyte. Cyclic voltammetry (CV), alternating-current (ac) voltammetry (ACV), and differential pulse voltammetry (DPV) were used for the electrochemical characterization of complex $\mathbf{1}^{4+}$.

Two UV−visible spectroelectrochemical configurations were used:

(a) Transmittance spectroelectrochemical measurements were performed at selected potentials in a quartz thin-layer cell containing a gold minigrid as the working electrode. The thin-layer compartment is placed inside a 1-cm-path-length cuvette containing ca. 0.5 mL of $\mathbf{1}^{4+}$ solution (50−100 μM). The $\mathbf{1}^{4+}$ solution filled the thin-layer space by capillary action, and this liquid thin layer was spectroscopically probed by using a diode-array spectrometer (Hewlett-Packard model 8453). The counter electrode (platinum wire) and the Ag/Ag^+ quasi-reference electrode were laterally placed in the quartz cuvette next to the thin-layer compartment.

(b) Normalized differential reflectivity in the form of $\delta R/R$-potential profiles was conducted during a slow potential scan with superimposed potential modulation (small-amplitude, sinusoidal waveform). Monochromatic light (wavelength chosen to be characteristic of the species being probed) is reflected off a mirror-polished platinum disk electrode and focused onto a photomultiplier operating at constant current set by a feedback system and a programmable power supply. ACV was used along with $\delta R/R$ measurements. After demodulation with a lock-in amplifier, the rectified ac and optical ac responses (normally the in-phase component) were monitored as a function of the electrode potential. The optical signal generated by the ac modulation can be represented by eq 1,[36] in which R is the reflectance, A is the absorbance, and E is the applied potential.

$$\frac{\delta R}{R} \propto \frac{1}{R}\frac{\delta R}{\delta E} = -\frac{1}{R}\frac{\delta A}{\delta c_{int}}\frac{\delta c_{int}}{\delta E} \quad (1)$$

The normalized $\delta R/R$ signal in expression (1) is proportional to $1/R\ \delta R/\delta E$ and increases with δE. The magnitude of $1/R\ \delta R/\delta E$ depends on both the kinetic capability of a particular species to follow the potential modulation and its extinction coefficient. Changes of the interfacial concentration (δc_{int}) at the characteristic wavelength of a specific species as originated by the δE potential perturbation are observed through a corresponding absorbance (A) change. The working electrode provides the potential modulation (source and sink of electrons) and doubles as a reflecting mirror for the optical signal.[36,37]

The molecular and electronic structure calculations of $\mathbf{1}^{4+}$ and $\mathbf{2}^{4+}$ were performed with density functional theory (DFT) using the *Gaussian03*[38] program package. We used the B3LYP functional and chose a cc-pVDZ basis set for hydrogen, carbon, and nitrogen and a LanL2DZ basis set for ruthenium. Because of the large size of the complexes and the number of atoms involved, solvent effects were first modeled by single-point calculations based on the gas-phase-optimized structures using the polarizable continuum model in acetonitrile. The orbital analysis was completed with *Gaussview*.[38]

Synthesis. *10,11-Diaminodipyrido[3,2-a:2′,3′-c]phenazine (10,11-Diaminodppz).* A mixture of 2.00 g (6 mmol) of 11-nitrodppz[39] and 10 g (0.14 mol) of hydroxylamine hydrochloride dissolved in 100 mL of ethanol was refluxed under nitrogen. A solution of KOH (20 g, excess) in methanol (100 mL) was then added dropwise during heating. After heating overnight, the mixture was left to stand for about 6 h, and then the precipitate was filtered, washed with water, and dried under vacuum to give 1.15 g (54% yield) of the desired compound. Mp: 155 °C. ^{1}H NMR (ppm, DMSO-d_6, 500 MHz): δ 5.59 (s, 2H, NH_2), 5.62 (s, 2H, NH_2), 7.51 (s, 2H), 7.85 (overlapped quartet, J_{HH} = 10.0 and 5.0 Hz, 2H), 9.07 (dd, J_{HH} = 10.0 and 5.0 Hz, 1H), 9.11 (dd, J_{HH} = 9.8 and 5.2 Hz, 1H), 9.39 (dd, J_{HH} = 10.0 and 3.5 Hz, 1H), 9.79 (dd, J_{HH} = 10.0 and 3.5 Hz, 1H). ESI-MS: m/z 313 (MH^+). Anal. Calcd for $C_{18}H_{12}N_6$: C, 69.22; H, 3.87; N, 26.91. Found: C, 68.87; H, 3.51; N, 26.87.

9,12,21,22-Tetraazatetrapyrido[3,2-a:2′,3′-c:3″2″-m:2‴,3‴-o]pentaphene (tatppα). A mixture of 100 mg (0.32 mmol) of 10,11-diaminodppz and 150 mg (0.71 mmol) of phendione (dissolved in minimal amount of chloroform) was added to 25 mL of glacial acetic acid and refluxed for 12 h, during which time a precipitate forms. The mixture was cooled and filtered and the precipitate washed successively with 10 mL of acetic acid, methanol, and chloroform. The solid was then dried in vacuo at 50 °C. Yield: 153 mg (99% based on diaminodppz). The product was sparingly soluble in all common solvents. NMR data can be obtained using a mixture of TFA and $CDCl_3$. Mp: 235 °C (dec). ^{1}H NMR (ppm, 1 M CF_3COOD in $CDCl_3$, 500 MHz): δ 8.40 (q, J_{HH} = 8.8 and 4.5 Hz, 2H), 8.51 (q, J_{HH} = 8.8 and 4.5 Hz, 2H), 8.87 (s, 2H), 9.41 (dd, J_{HH} = 9.8 and 4.7 Hz, 2H), 9.45 (dd, J_{HH} = 9.2 and 4.8 Hz, 2H), 10.30 (d, J_{HH} = 9.8 Hz, 2H), 10.56 (d, J_{HH} = 9.8 Hz, 2H). ESI-MS: m/z 487 (MH^+). Anal. Calcd for $C_{30}H_{14}N_8$: C, 74.07; H, 2.90; N, 23.03. Found: C, 73.77; H, 2.81; N, 22.87.

*[(phen)$_2$Ru(tatppα)Ru(phen)$_2$][PF$_6$]$_4$ ([**1**][PF$_6$]$_4$).* A mixture of 100 mg (0.21 mmol) of tatppα and 260 mg (0.49 mmol) of $Ru(phen)_2Cl_2$ was suspended in 30 mL of ethanol and 30 mL of water and refluxed for 7 days. The mixture was then stored at 4 °C for 12 h and filtered. The addition of aqueous NH_4PF_6 resulted in a precipitate, which was isolated by filtration and washed with 10 mL of water (3×) and 10 mL of ethanol (3×). The product was further purified by repeated metathesis between Cl^- and PF_6^- salts. The Cl^- salt was prepared from the PF_6^- salt by adding a concentrated solution of *n*-tetrabutylammonium chloride in acetone to a concentrated solution of the $2(PF_6)_4$ salt in acetone. The precipitate was filtered and washed with 5 mL of acetone (3×) and 10 mL of diethyl ether. The Cl^- salt was converted back to the PF_6^- salt by adding a concentrated solution of ammonium hexafluorophosphate in water to the Cl^- salt dissolved in a minimum amount of water. The precipitate was filtered and washed with 10 mL of water (3×), 10 mL of ethanol, and 10 mL of diethyl ether. This metathesis sequence was repeated three times. The final product is hygroscopic and was dried at 120 °C for 4 h. Yield: 200 mg (47%). Mp: >250 °C (dec). ^{1}H NMR (ppm, CD_3CN, 500 MHz): δ 7.67 (m, J_{HH} = 10.0 and 5.0 Hz, 8H), 7.8 (dd, J_{HH} = 8.0 and 5.4 Hz, 2H), 7.91 (dd, J_{HH} = 8.4 and 5.6 Hz, 2H), 8.03 (d, J_{HH} = 5.4 Hz, 4H), 8.19 (q, J_{HH} = 4.2 Hz, 4H), 8.25 (d, J_{HH} = 2.0 Hz, 4H), 8.27 (s, 8H), 8.63 (d, J_{HH} = 9.0 Hz, 8H), 8.81 (s, 2H), 9.79 (dd, J_{HH} = 8.3 and 1.0 Hz, 2H), 10.12 (dd, J_{HH} = 8.3 and 1.0 Hz, 2H). ESI-MS: m/z 1989 (M), 1844 ($[M - PF_6]^+$), 850 ($[M - 2PF_6]^{2+}$), 518 ($[M - 3PF_6]^{3+}$), 352 ($[M - 4PF_6]^{4+}$). Anal. Calcd for $C_{78}H_{46}N_{16}F_{24}P_4Ru_2 \cdot 2H_2O$: C, 46.25; H, 2.48; N, 11.06. Found: C, 46.15; H, 2.59; N, 11.06. The waters of crystallization were detected by NMR in dry CD_3CN and shown by integration to be 2 H_2O per $\mathbf{1}[PF_6]_4$. Thermogravimetric analysis revealed that these waters were tightly bound and not lost until the sample was heated over 200 °C.

RESULTS

Synthesis. The tatppα ligand is obtained in 64% yield via the condensation reaction of 10,11-diaminodppz and phendione. A similar reaction between 11,12-diaminodppz and phendione yields the linear ligand tatppβ in comparable yields. The key compounds in the preparation of tatppα and tatppβ are 10,11-diaminodppz and 11,12-diaminodipyrido[3,2-*a*:2′,3′-*c*]phenazine, respectively. While the latter was easily obtained from 1,2-diamino-4,5-dinitrobenzene and phendione,[35] the former was previously unreported. We intended to introduce the amino function at the 10th position via a base-induced amination reaction to form 10-amino-11-nitrodppz and then reduce to the diamine; however, some

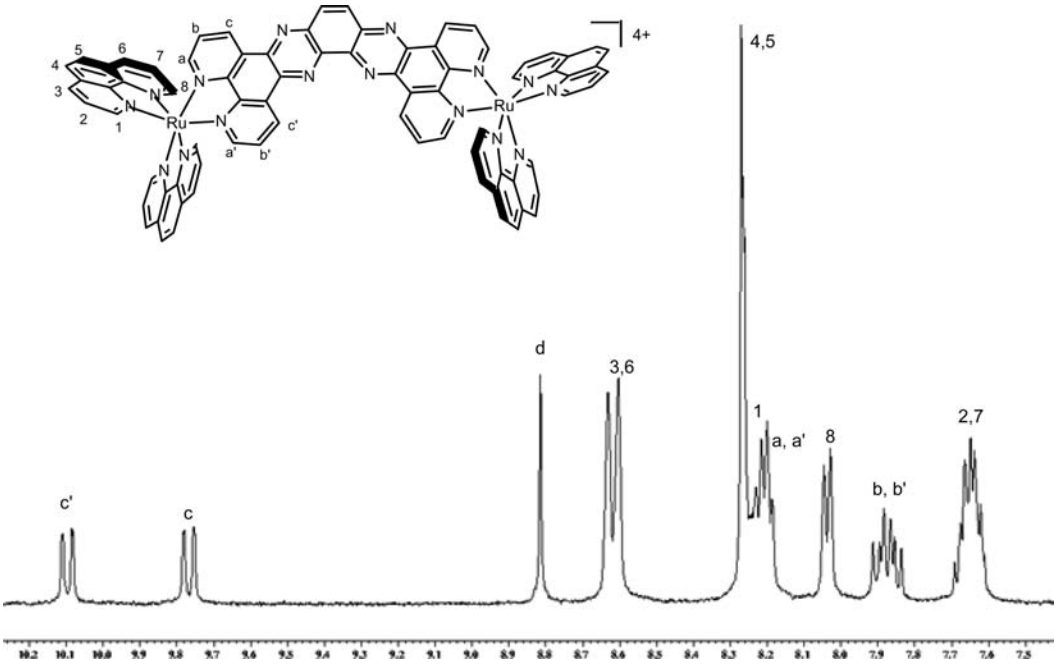

Figure 2. ^{1}H NMR spectrum of the complex $[\mathbf{1}][PF_6]_4$ in CD_3CN.

reduction of the nitro group was apparent in the first step. We then discovered that the desired diamine could be obtained in one step from 11-nitrodppz in 54% yield using a slight modification of the Pietra and Casiraghi procedure[40] for the reductive amination of arylnitro compounds. 11-Nitrodppz was readily obtained in good yield (87%) via the condensation of 1,2-diamino-4-nitrobenzene with phendione.

The structure of tatppα was confirmed by ^{1}H NMR spectroscopy and electrospray ionization mass spectrometry (ESI-MS). Because of the poor solubility of tatppα, its ^{1}H NMR spectrum was obtained in a mixture of $CDCl_3$ and trifluoroacetic acid (TFA). The ligand tatppα has C_{2v} point group symmetry; two AMX spin-coupled systems are seen corresponding to the phen outer (H_a, H_b, and H_c) and inner ($H_{a'}$, $H_{b'}$, and $H_{c'}$) hydrogen atoms. The two symmetrically equivalent hydrogen atoms (H_d) on the central benzene ring appear as a singlet at 8.87 ppm. The downfield shift is typical of hydrogen atoms adjacent to pyrazine-like nitrogen atoms in these compounds. The linear ligand tatppβ has D_{2h} point group symmetry and shows only four peaks with the central H_d hydrogen atoms shifted even further downfield at 9.79 ppm because of the positioning between two pyrazine-like nitrogen atoms.[41] ESI-MS for tatppα showed a monoprotonated parent ion peak $[M + H]^+$ at m/z 487.

The dinuclear complex $\mathbf{1}^{4+}$ was prepared in 44% yield by refluxing a suspension of tatppα with 2.1 equiv of $Ru(phen)_2Cl_2$ in 1:1 ethanol−water for 7 days, which is analogous to the preparation of $\mathbf{2}^{4+}$.[41] This complex is freely soluble in MeCN as the hexafluorophosphate salt and in water as the chloride salt. The synthetic method of preparation does not control the absolute stereochemistry at the two Ru^{II} chiral centers, and thus the product $\mathbf{1}^{4+}$ is actually a mixture of diastereomers. As has been seen with similar dinuclear complexes of tpphz, tatppβ, and tatpq, these diastereomers often have identical NMR spectra owing to the large distance between stereocenters.[42,43] Similarly, the electrochemical and photophysical properties are essentially identical.

The ^{1}H NMR spectrum of $\mathbf{1}^{4+}$ in CD_3CN is shown in Figure 2, and it is readily apparent from the simplicity of the data that the diastereomers are indistinguishable by NMR. The 2-fold symmetry of the complex is also apparent, with two sets of three peaks corresponding to the tatppα outer H_a, H_b, and H_c and inner $H_{a'}$, $H_{b'}$, and $H_{c'}$ peaks plus a singlet for H_d observed. H_c and $H_{c'}$ are found the furthest downfield because of their positioning over the pyrazine nitrogen atoms. The outer position H_c is assigned as such by comparison with the single doublet seen for H_c in $\mathbf{2}^{4+}$ at 9.70 ppm. The central H_d peak seen at 9.60 ppm in $\mathbf{2}^{4+}$ is observed at 8.82 ppm in $\mathbf{1}^{4+}$, reflecting the decrease in the number of nearest-neighbor aza nitrogen atoms in $\mathbf{1}^{4+}$ relative to $\mathbf{2}^{4+}$. Coupled systems were assigned by COSY analysis.

The ESI-MS spectrum obtained for $\mathbf{1}^{4+}$ shows peaks consistent with the following parent ions: $[\mathbf{1} - 1PF_6]^+$ at m/z 1843, $[\mathbf{1} - 2PF_6]^{2+}$ at m/z 850 (the highest peak), $[\mathbf{1} - 3PF_6]^{3+}$ at m/z 518, and $[\mathbf{1} - 4PF_6]^{4+}$ at m/z 352. These data in conjunction with the elemental analyses and NMR data prove the structure of the complex.

Electronic Spectra and Structure. The electronic absorption spectra of the zinc(II) adduct of tatppα and the ruthenium(II) complex $\mathbf{1}^{4+}$ in acetonitrile are overlaid in Figure 3a, and the electronic absorption spectra of the zinc(II) adduct of tatppβ and the ruthenium(II) complex $\mathbf{2}^{4+}$ in acetonitrile are overlaid in Figure 3b. Both tatppα and tatppβ ligands are insoluble in common solvents; however, complexation with excess Zn^{II} ions solubilizes these ligands in acetonitrile and allow viewing the ligand-centered (LC) absorption bands. Coordination of Zn^{II} is expected to perturb these LC transitions; however, the magnitude of such perturbations is expected to be small. The Zn(tatppβ) adduct (Figure 3b) shows two strong, sharp absorptions centered at 325 and 445 nm, with the latter peak showing a vibrational structure. The Zn^{II}(tatppα) adduct shows a sharp peak in the same region that is centered at 356 nm, with a smaller shoulder peak at 321 nm. All of these peaks are intraligand (or LC) peaks and are only slightly perturbed upon switching

dx.doi.org/10.1021/ic2006698 |*Inorg. Chem.* 2011, 50, 9318–9328

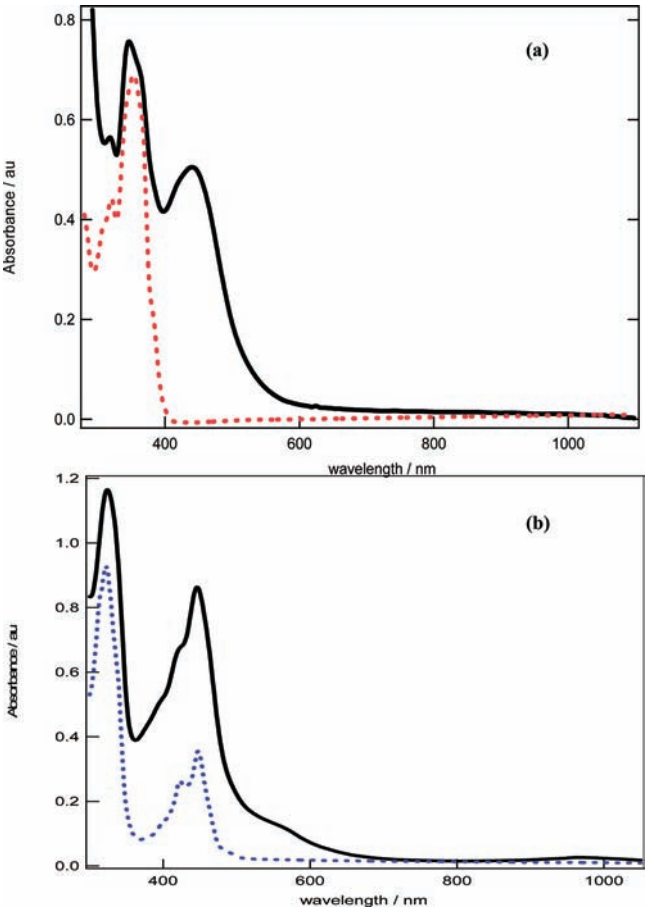

Figure 3. Comparison of UV−visible spectra (MeCN) of (a) 20 μM tatppα and excess $Zn(BF_4)_2$ (dotted red line) and the dinuclear complexes $\mathbf{1}^{4+}$ (solid black line) and (b) 20 μM tatppβ and excess $Zn(BF_4)_2$ (dotted blue line) and the dinuclear complexes $\mathbf{2}^{4+}$ (solid black line).

from Zn^{II} to Ru^{II} coordination. As seen in Figure 3a, the ruthenium complex $\mathbf{1}^{4+}$ shows a broad, intense MLCT transition centered at 441 nm and a tatppα LC transition at 356 nm, which is of intensity and shape similar to those of the zinc(II) adduct. A similar situation is seen in the spectrum of $\mathbf{2}^{4+}$; however, in this case, the structured LC transitions at 445, 422, and 405 nm are overlapped with the MLCT band at 445 nm, leading to a spectrum that is essentially the sum of the two contributing components. The tatppβ LC band at 325 nm is shifted to 330 nm and is slightly more intense in $\mathbf{2}^{4+}$ but is otherwise unchanged. The spectrum of $\mathbf{2}^{4+}$ has two additional features not seen in either the Zn(tatppβ) adduct or the related tatppα complexes (zinc or ruthenium). These are a significantly broad and reasonably intense peak appearing as a shoulder at 550 nm and a second weaker and also broad peak at 950 nm.

Electrochemistry. Representative cyclic voltammograms spanning the electroreduction region of complex $\mathbf{1}^{4+}$ are shown in Figure 4a, while DPVs in the same potential region comparing $\mathbf{1}^{4+}$ and $\mathbf{2}^{4+}$ are presented in Figure 4b. The half-wave potential data are collected in Table 1, which also provides the respective reduction potentials for $\mathbf{2}^{4+}$ and $[Ru(phen)_3]^{2+}$, obtained under the same conditions. For the cathodic processes, three independent cyclic voltammograms were recorded from 0.1 V (open-circuit potential) down to three selected negative switching

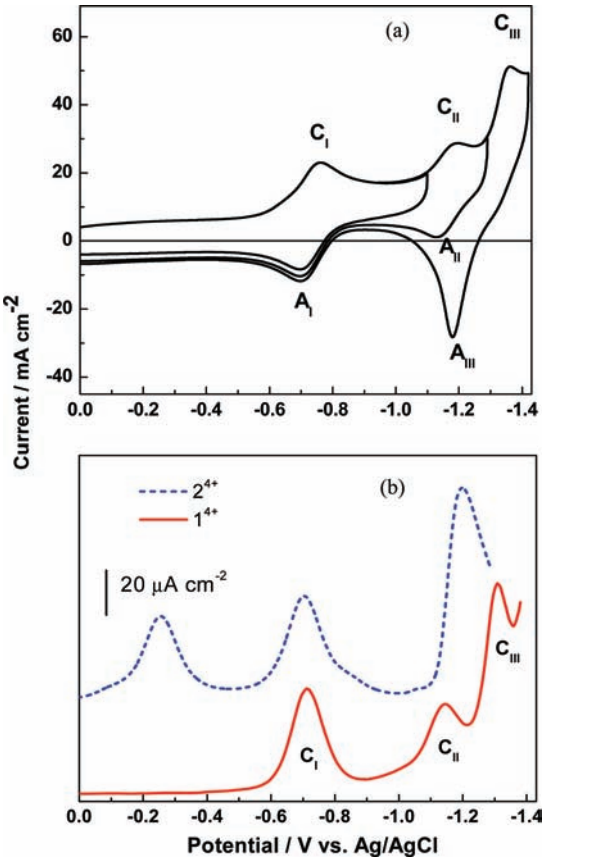

Figure 4. (a) Cyclic voltammograms for the electroreduction of $\mathbf{1}^{4+}$ (40 μM) on a glassy carbon electrode (diameter = 1.5 mm) in MeCN containing 0.1 M $TBAPF_6$. Three CV runs at 50 mV/s are shown with different negative potential limits (−1.10, −1.30, and −1.42 V). After each scan, the electrode was repolished and started from the open-circuit potential (0.1 V). Three quasi-reversible redox processes (C_I/A_I, C_{II}/A_{II}, and C_{III}/A_{III}) are shown clearly by using the three selected potential windows. (b) Differential pulse voltammograms comparing the electroreductions of $\mathbf{1}^{4+}$ (solid red line) and $\mathbf{2}^{4+}$ (dashed blue line) in MeCN containing 0.1 M $TBAPF_6$. Potential pulse amplitude = 0.05 V, step size = 0.004 V, pulse duration = 0.05 s, and pulse period = 0.2 V.

Table 1. Redox Potentials for $\mathbf{1}^{4+}$ and $\mathbf{2}^{4+}$ Complexes

	reduction (V)[a]		oxidation (V)[a]
complex	first	second	$Ru^{2+/3+}$
$[(phen)_2Ru(tatppα)Ru(phen)_2]^{4+}$ ($\mathbf{1}^{4+}$)	−0.73	−1.14	1.35
$[(phen)_2Ru(tatpp\beta)Ru(phen)_2]^{4+}$ ($\mathbf{2}^{4+}$)	−0.22	−0.71	1.35
$[Ru(phen)_3]^{2+}$	−1.38	−1.52	1.36

[a] Potentials are reported versus a Ag/AgCl (3.0 M KCl) reference electrode and obtained from CV and DPV measurements performed in acetonitrile containing 0.1 M $TBAPF_6$.

potentials (−1.10, −1.30, and −1.42 V, respectively). The data depict the three successive redox processes in complex $\mathbf{1}^{4+}$, and they are indicated as C_I/A_I, C_{II}/A_{II}, and C_{III}/A_{III} (C standing for cathodic and A for anodic processes, respectively). The first cyclic voltammogram, with a switching potential of −1.10 V, encompasses the redox process C_I/A_I, while the second has the reversing potential at −1.30 V, chosen to detect peaks C_{II} and A_{II}, with the latter peak being otherwise masked by the

dx.doi.org/10.1021/ic2006698 |Inorg. Chem. 2011, 50, 9318–9328

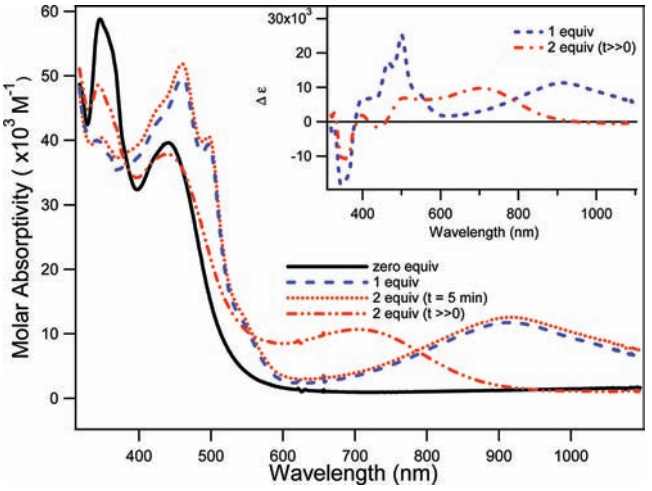

Figure 5. Absorption spectra of $\mathbf{1}^{4+}$ (black solid line) after the addition of 1.2 equiv of cobaltocene (blue dashed line) and after an additional 1.0 equiv of cobaltocene (2.2 equiv in total). Red dotted line at $t = \sim 5$ min after mixing and dash-dotted red line for $t > 12$ h. The final concentration of complex $\mathbf{1}^{4+/3+/2+}$ in each cuvette was 15 μM. Inset: Difference absorption spectra corresponding to the addition of 1 (dashed blue line) and 2 (dashed red line) equiv of cobaltocene to complex $\mathbf{1}^{4+}$ (taken as a reference for the subtraction).

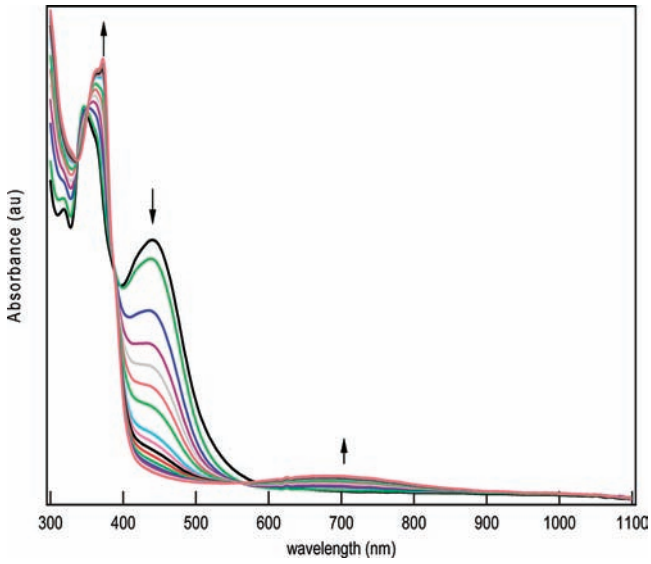

Figure 6. Spectroelectrochemistry during the electrooxidation of $\mathbf{1}^{4+}$ (80 μM) in MeCN containing 0.1 M $TBAPF_6$. For the electrooxidation ($Ru^{2+} \rightarrow Ru^{3+}$), a potential step of 0.0 to +1.6 V was applied for 180 s. Spectral acquisition was performed in a quartz thin-layer cell.

contribution of the next redox process. Because the third voltammogram goes down to −1.42 V to include process C_{III}, the back scan shows the oxidation of peak A_{III}. Clearly, each individual cyclic voltammogram in Figure 4 leads to the detection of interrelated peaks. The $Ru^{3+/2+}$ redox process features a single reversible wave located at $E_{1/2}$ = 1.35 V with at least twice the amplitude of the C_I/A_I and C_{II}/A_{II} processes, suggesting two electrons (data not shown).

As can be seen from Figure 4b, the first reduction $\mathbf{1}^{4+/3+}$ occurs at a potential 500 mV more negative than that observed for the $\mathbf{2}^{4+/3+}$ couple. Similarly, the second reduction, $\mathbf{1}^{3+/2+}$, is found at a potential ~430 mV more negative than that for the related $\mathbf{2}^{3+/2+}$ couple. Clearly, the "bent" tatppα structure leads to higher-energy acceptor orbitals than those in the linear tatppβ ligand.

Spectral Characterization of the Reduced and Oxidized Forms of $\mathbf{1}^{4+}$. To characterize the spectral signature of the reduced congeners of $\mathbf{1}^{4+}$, stoichiometric reduction of the complex was performed with cobaltocene in acetonitrile under anaerobic conditions, and the results are shown in Figure 5. Cobaltocene is a strong one-electron reducing agent, $Co(Cp)_2^{+/0}$ = −1.15 V vs Ag/AgCl/saturated KCl,[44] and is thermodynamically capable of generating $\mathbf{1}^{3+}$ and potentially $\mathbf{1}^{2+}$ ($E_{1/2}$ of −0.73 and −1.14 V, respectively). The reduction of $[Ru(phen)_3]^{2+}$ to $[Ru(phen)_3]^{+}$ is observed at even more negative potentials ($E_{1/2}$ = −1.38 V), and thus we do not anticipate that cobaltocene will drive reduction reactions associated with the formation of the phen radical anion. The cobaltocenium ion produced is very light yellow in color (λ_{max} = 409 nm; ε = 200)[45] and adds no appreciable absorption to the visible and near-IR portions (350−1100 nm) of the absorption spectra.

The absorption spectra of the singly reduced $\mathbf{1}^{\bullet 3+}$ are shown in Figure 5 and were generated by the addition of a slight stoichiometric excess of $Co(Cp)_2$ (1.2 equiv). As the peak at 930 nm reaches a maximum at this stoichiometry, we attribute the need for an excess of cobaltocene as being due to adventitious O_2. Because this kind of titration is carried out under dilute conditions (15 μM $\mathbf{1}^{4+}$) for optical transparency, as little as 24 ppb O_2 would account for this discrepancy, and this level of O_2 contamination is not possible to remove using glovebox techniques. Complex $\mathbf{1}^{\bullet 3+}$ is characterized by the appearance of two rather sharp spectral features at 460 and 505 nm, a broad band peaking at ca. 930 nm, and bleaching of the band at 356 nm (Figure 5, blue dashed line). The broad, low-energy peak at 890 nm is very broad and is consistent with the formation of a delocalized radical anion on the tatppα ligand. The analogous radical anion in $\mathbf{2}^{\bullet 3+}$ also shows broad, low-energy peaks at 855 and 965 nm, which in this case is simply one peak split by vibronic coupling.[25,46]

Initially, the addition of a second 1 equiv of $Co(Cp)_2$ to $\mathbf{1}^{\bullet 3+}$ does not yield much change in the spectrum (Figure 5, red dotted line); however, when the solution was then allowed to stand overnight, subsequent spectral changes were observed, as shown in Figure 5 (red dash-dotted line). This new spectrum shows a broad band peaking at 700 nm attended by bleaching of the 930, 460, and 505 nm bands and a partial recovery of the 356 nm band. These spectral changes are very similar to those observed upon the reduction of $\mathbf{2}^{\bullet 3+}$ to $\mathbf{2}^{2+}$ and therefore are presumably related to the formation of the doubly reduced species $\mathbf{1}^{2+}$. However, unlike the fast and facile reduction of $\mathbf{2}^{\bullet 3+}$ to $\mathbf{2}^{2+}$ with cobaltocene, the reduction of $\mathbf{1}^{\bullet 3+}$ with cobaltocene is slow. We are unsure as to why this process is so slow but note that, because of a shift in the reduction potentials, this reaction is essentially thermoneutral. Attempts to use stronger reducing agents, such as decamethylcobaltocene, failed to give data that were any more informative than that shown. As discussed later, the slowness may be due, in part, to dimerization of the radical $\mathbf{1}^{\bullet 3+}$, which was not observed in our earlier studies of the related radical $\mathbf{2}^{\bullet 3+}$.

Spectroelectrochemistry. Spectral changes brought about by the electrooxidation of the ruthenium centers in $\mathbf{1}^{4+}$ to $\mathbf{1}^{5+}$ and ultimately $\mathbf{1}^{6+}$ are shown in Figure 6. The first spectrum at the open circuit (black solid line) is seen to progressively decrease the MLCT band (445 nm) as the electrolysis time increases. This

dx.doi.org/10.1021/ic2006698 |*Inorg. Chem.* 2011, 50, 9318–9328

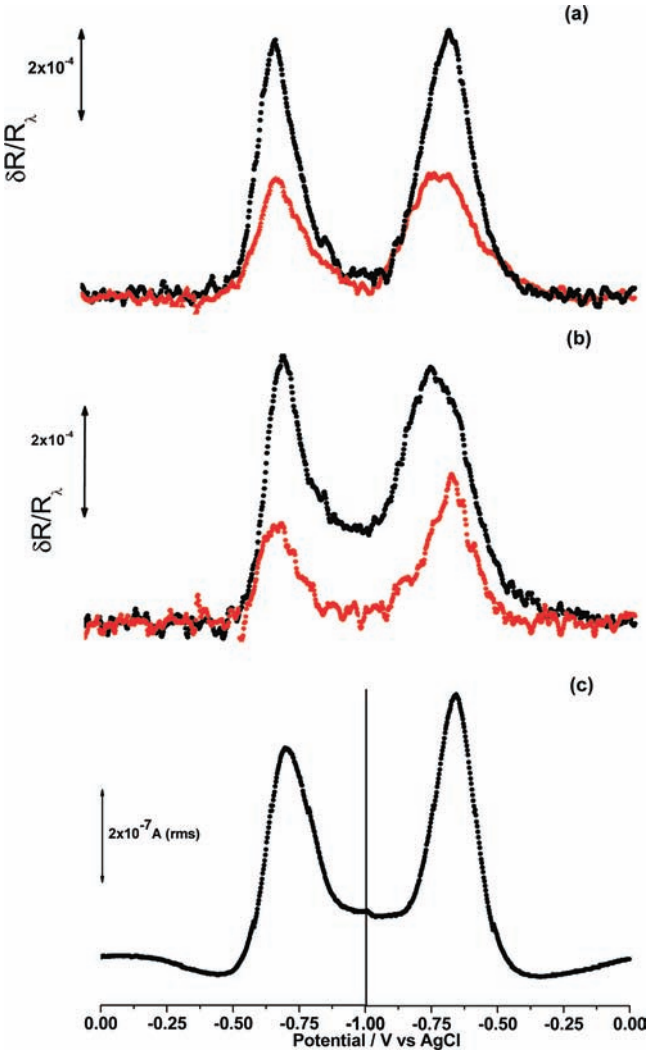

Figure 7. Effect of the modulation frequency on the $\delta R/R$ potential curves for 30 μM $\mathbf{1}^{4+}$ at 850 (a) and 460 nm (b). The corresponding ac voltammogram is shown in part c. Potential window = 0.0/−1.0 V and scan rate = 1 mV s^{-1}. Switching potentials are seen at the center of each graph. $\delta R/R$ signals of 6 and 11 Hz are shown in black and red, respectively.

bleaching is continual and indicative of a simultaneous oxidation of the two ruthenium(II) centers. Indeed, only one peak is seen in the cyclic voltammogram for this process, indicating that the two ruthenium(II) centers are weakly coupled if at all. A new broad and relatively weak band grows in at 690 nm, which appears to be common in ruthenium(3+) tris(diimine) complexes.[47−49] Finally, it is observed that the LC band at 356 nm increases in intensity accompanied by a slight red shift to 368 nm.

Figures 7 and 8 show differential reflectivity, $\delta R/R$, profiles at selected wavelengths chosen to track the electroreduced species: 850 nm (this is the longest wavelength the instrument would function at) and 460 nm for the first electron uptake ($\mathbf{1}^{\bullet 3+}$) and 650 nm for the doubly reduced $\mathbf{1}^{2+}$ species. Although the peak for $\mathbf{1}^{2+}$ is at 700 nm (Figure 5), 650 nm was chosen to follow the appearance of $\mathbf{1}^{2+}$ because there is less overlap with the broad 930 nm peak from the singly reduced species. All plots are presented with the potential axis unfolded (i.e., the switching potential being at the center of the *x* axis); processes occurring on

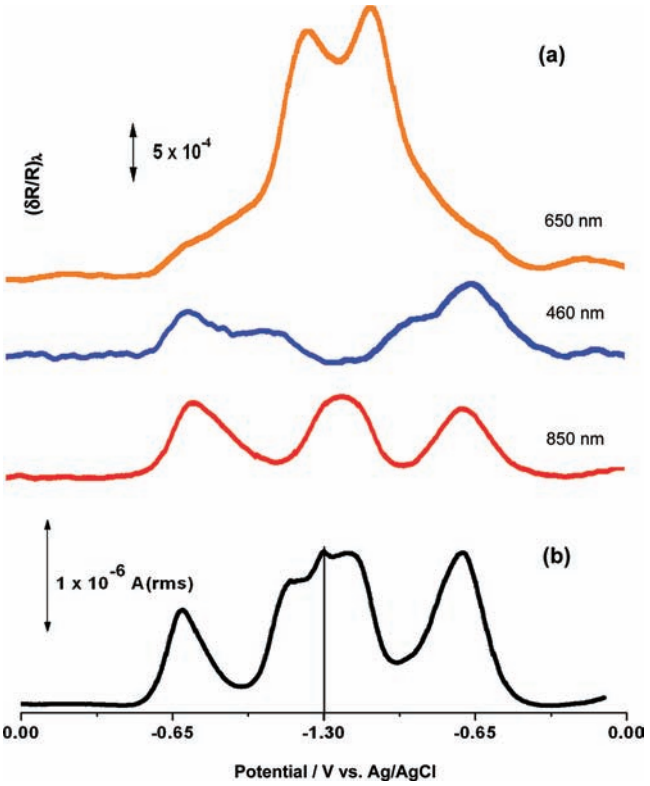

Figure 8. (a) $\delta R/R$ potential curves for 45 μM $\mathbf{1}^{4+}$ at 650 (top), 460 (center), and 850 nm (bottom). The corresponding ac voltammogram is shown in part b. Potential window = 0.0/−1.3 V and ac frequency = 6 Hz. Other experimental conditions are as in Figure 7.

the negative potential scan are shown on the left side, and those during the back scan are on the right side. The figures also contain the corresponding ac voltammograms.

Figure 7 shows the effect of the ac frequency (6 and 11 Hz) on the differential reflectivity, $\delta R/R$ (Figure 7a,b) and ac current (Figure 7c) profiles of 30 μM $\mathbf{1}^{4+}$ for the C_I/A_I process (switching potential of −1.0 V) corresponding to the $\mathbf{1}^{4+/\bullet 3+}$ couple. The intensity of $\delta R/R$ increases as the frequency decreases for both 850 (Figure 7a) and 460 nm (Figure 7b) profiles, as is expected for an electron transfer under diffusion control (Warburg region). While $\delta R/R$ data at 850 nm show a single peak on the forward and returning scans at both frequencies, the $\delta R/R$ profile at 460 nm indicates that this redox process is more complicated than first presumed. The tailing of this peak on the forward scan and the broad double peak on the back scan can be indicative of subsequent chemical reactions. This deviation from ideal electrochemical behavior is most pronounced at the lower modulation frequency, 6 Hz (Figure 7b).

Figure 8a corresponds to $\delta R/R$ profiles of $\mathbf{1}^{4+}$ at 6 Hz at three wavelengths (850, 460, and 650 nm, respectively), and in this case, both the C_I/A_I ($\mathbf{1}^{4+/\bullet 3+}$) and C_{II}/A_{II} ($\mathbf{1}^{\bullet 3+/2+}$) processes are covered with a switching potential of −1.3 V. The corresponding ac voltammogram is shown in Figure 8b. The most relevant findings from the optical data are as follows: (1) the $\delta R/R$ signal at 850 nm presents a single peak (Figure 8a, bottom) encompassing voltammetric peak C_I, and the profile is retraced during the return scan. (2) $\delta R/R$ at 460 nm (Figure 8a, center) presents a peak coinciding with that at 850 nm (Figure 8a, bottom) followed by a well-defined shoulder that disappears completely at

dx.doi.org/10.1021/ic2006698 |*Inorg. Chem.* 2011, 50, 9318–9328

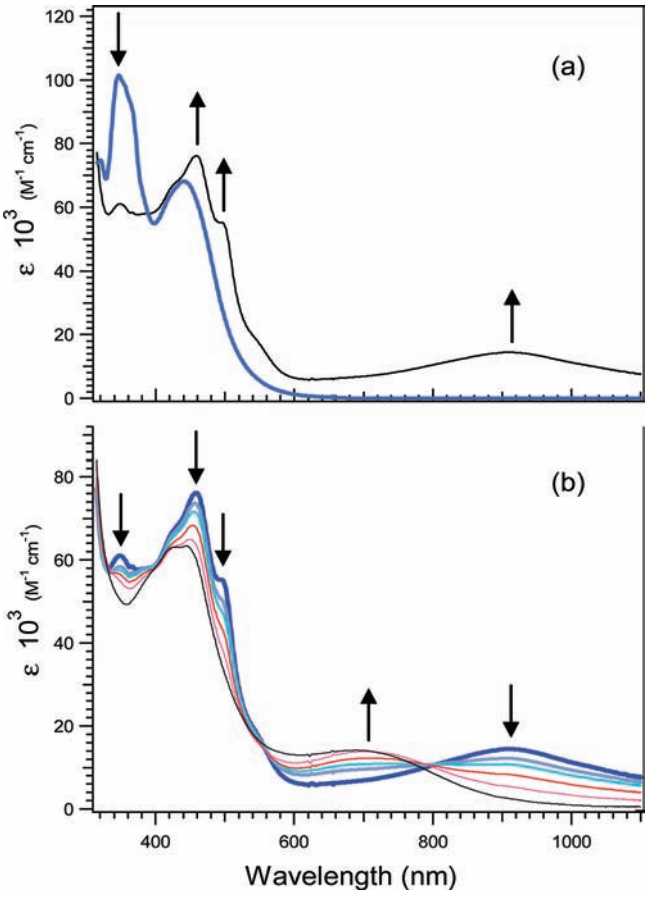

Figure 9. Evolution of the absorption spectrum of $\mathbf{1}^{4+}$ during photolysis of 16 μM $\mathbf{1}^{4+}$ in MeCN containing 0.25 M TEA: (a) at 0 and 2 s irradiation; (b) at subsequent times during a period of 30 min. Light irradiation with a 100 W tungsten lamp.

the end of the scan (−1.3 V). Again the profile is retraced during the return scan. (3) $\delta R/R$ at 650 nm (Figure 8a, top) shows the uptake of the second electron at the C_{II} peak. The shoulder preceding this peak is a result of the appearance of the broad 850 nm peak in the first reduction, which has a measurable intensity at 650 nm. Similarly, the increase in the absorbance at 850 nm at the most negative potentials is an artifact from the growth of the broad 690 peak during the C_{II} process. A mirrorlike profile for 650 nm is obtained during the back scan, showing the electrochemical quasi-reversibility of this process. These $\delta R/R$ potential profiles, along with the other spectral data, will be the basis for determination of the complete electroreduction mechanism of complex $\mathbf{1}^{4+}$, which is presented in the discussion.

Photochemistry of Complex $\mathbf{1}^{4+}$. Visible-light irradiation of complex $\mathbf{1}^{4+}$ in the presence of TEA and under anaerobic conditions causes two sequential changes to the initial absorption spectrum of $\mathbf{1}^{4+}$ (Figure 9). The first process, shown in Figure 9a, occurs very fast (~2 s irradiation) and shows the appearance of a very broad absorption centered at ca. 890 nm as well as structured bands at 460 and 505 nm. The LC band at 356 nm is bleached in the process. Despite the swiftness of this first process, it is undoubtedly a photochemical process because no changes to the initial spectrum were seen until the sample was irradiated. If air is introduced at this point, the starting spectrum is rapidly regenerated, indicating that the first photochemical process is both facile and reversible.

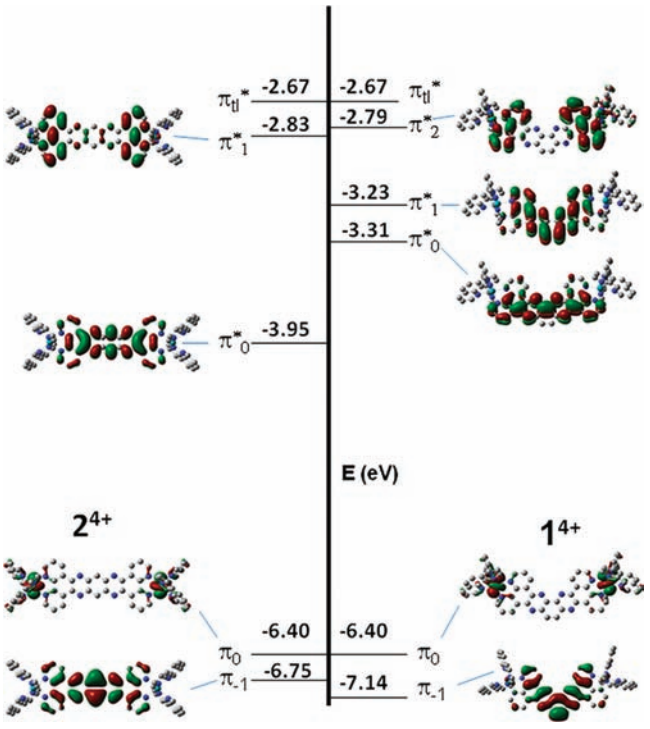

Figure 10. MO energy diagrams of the relevant frontier MOs for complexes $\mathbf{1}^{4+}$ and $\mathbf{2}^{4+}$ calculated using DFT.

A second photoproduct was observed at longer irradiation times, taking a total of 30 min to reach the final spectrum, as shown in Figure 9b. The arrows indicate the bands' evolution with time, and as can be seen, the second photoprocess bleaches the bands at 890 nm and the two structured bands at 460 and 505 nm. Concurrently, the appearance of a new absorption band at 690 nm is observed; however, there is no clear isosbestic point between the 890 and 690 nm bands, suggesting that this conversion might involve more than one step and/or species. Exposure of this solution to O_2 also regenerates $\mathbf{1}^{4+}$; however, in this case, the process is very slow and can take up to 12 h, suggestive of a more complicated chemical process.

These spectral changes seen in the photochemistry for $\mathbf{1}^{4+}$ mirror those seen upon reduction with 1 and then 2 equiv of cobaltocene and are similar to those seen for the photoreduction of $\mathbf{2}^{4+}$ to $\mathbf{2}^{\bullet 3+}$ and then to $\mathbf{2}^{2+}$. In the case of $\mathbf{2}^{4+/3+/2+}$, however, all of the processes are rapidly reversed upon exposure to air to regenerate $\mathbf{2}^{4+}$. In any case, the data strongly support the photochemical process as being associated with a one- and then two-electron reduction of the tatppα ligand in $\mathbf{1}^{4+}$. The slow photochemical response for the second electron uptake in $\mathbf{1}^{4+}$ is suggestive of some chemical stabilization of the photoreduced species.

DFT Calculations. DFT molecular orbital (MO) calculations have proven useful in describing the optical and redox properties of this class of complexes. An energy diagram, including pictures of the relevant frontier MOs for $\mathbf{1}^{4+}$ and $\mathbf{2}^{4+}$, is shown in Figure 10. The energies are calculated in electronvolts (eV), but these values are not absolute and should only be used for comparisons within the DFT model. The HOMOs for $\mathbf{1}^{4+}$ and $\mathbf{2}^{4+}$ are best described as Ru dπ orbitals (π_0) and are found at identical energies for both complexes. The acceptor orbitals are localized either on the bridging ligand (π_0^*, π_1^*, and π_2^* in $\mathbf{1}^{4+}$

dx.doi.org/10.1021/ic2006698 |*Inorg. Chem.* 2011, 50, 9318–9328

and π_0^* and π_1^* in $\mathbf{2}^{4+}$) or on the terminal phen ligands (π_{tl}^*). The relevant tatppα and tatppβ acceptor orbitals are largely localized either on the central pyrazine−benzene−pyrazine-like (pz−bz−pz) portions of the bridging ligands (π_0^* and π_1^* in tatppα and π_0^* in tatppβ) and or on the phen-like ends (π_2^* in tatppα and π_1^* in tatppβ). As has been described in dppz complexes as well as in $\mathbf{2}^{4+}$,[25,32] the broad overlapping absorbances in the 440−480 nm region of $\mathbf{1}^{4+}$ reflect MLCT transitions of the type Ru^{II} d$\pi \rightarrow$ phen π_{tl}^* and Ru^{II} d$\pi \rightarrow$ "phen-like" π_2^* transition. The lack of absorptions at lower energies shows that the electronic coupling between the Ru dπ HOMO and the bridging ligand "pz−bz−pz-like" orbitals (π_0^* and π_1^*) is very weak. This is understood, in part, by the lack of any appreciable π-orbital density on the tatppα coordinating nitrogen atoms in π_0^* and π_1^*. Kaim and co-workers[29] have described these "phen-like" orbitals as optical orbitals because of their predominant role in the ground-state optical properties.

In contrast, the lower-energy "pz−bz−pz-like" MOs appear to be directly involved in the redox behavior of both $\mathbf{1}^{4+}$ and $\mathbf{2}^{4+}$. The first reduction on $\mathbf{2}^{4+}$ at −0.22 V (vs Ag/AgCl) correlates well with the low energy of the LUMO (π_0^*), whereas the first reduction potential for $\mathbf{1}^{4+}$ is found to be ∼500 mV more negative (−0.73 V) and is indicative of the higher energy calculated for the LUMO (π_0^*) and LUMO+1 (π_1^*) for this complex. While these central acceptor orbitals are higher in energy than the LUMO for $\mathbf{2}^{4+}$, they are still lower in energy than the "phen-like" LUMO+2 (π_2^*). This correlation of the redox properties with the central pz−bz−pz LUMOs leads to a classification of these as the redox orbitals.

In $[Ru(phen)_3]^{2+}$, the redox and optical acceptor orbitals are the same. The reduction to form $[Ru^{II}(phen)_2(phen^{\bullet-})]^+$ occurs at −1.38 V, and MLCT optical excitation at ∼450 nm forms the $[Ru^{III}(phen)_2(phen^{\bullet-})]^{2+*}$ excited state, where the excited electron formally resides in the phen π^* orbital. As seen in the MO diagram, all of the "phen-like" MOs on tatppα and tatppβ are calculated to have energies very close to that of the phen LUMO (π_{tl}), which explains the MLCT bands in all of these complexes found in the same region.

The transitions in $\mathbf{1}^{4+}$ at 356 and 321 nm are assigned as LC $\pi_{-1} \rightarrow \pi_0^*$ and $\pi_{-1} \rightarrow \pi_1^*$ bands, respectively, with the π_{-1} orbital (shown in Figure 10) being the highest-energy tatppα-centered MO (HOMO−6 in the calculations for $\mathbf{1}^{4+}$). The same assignments can be made for the Zn^{II}(tatppα) adduct. The corresponding LC transitions at 445 and 321 nm in $\mathbf{2}^{4+}$ are assigned as $\pi_{-1} \rightarrow \pi_0^*$ and $\pi_{-1} \rightarrow \pi_1^*$ bands, respectively, with identical assignments also made for absorptions in the Zn^{II}-(tatppβ) adduct. A comparison of the energies of these transitions predicted by the DFT calculations is in good qualitative agreement with the observed spectra.

DISCUSSION

The dinuclear complexes $\mathbf{1}^{4+}$ and $\mathbf{2}^{4+}$ are regioisomers that differ only in the substitution pattern about the central benzene ring in the bridging ligand. In complex $\mathbf{2}^{4+}$, the linear tatppβ ligand is used, whereas for $\mathbf{1}^{4+}$, the "bent" tatppα ligand is used. As is seen, this structural change results in one key difference in their ground-state properties. The first and second reduction potentials of the tatppα ligand in $\mathbf{1}^{4+}$ are shifted to significantly more negative potentials than those found for tatppβ in $\mathbf{2}^{4+}$. This shift is predicted by MO calculations, which show that the energy of the tatppα LUMO those appreciably higher than that in tatppβ and appears to be a consequence of directing two of the central nitrogen lone pairs toward each other, causing some lone pair−lone pair repulsion. Reduction only exacerbates this repulsion. Importantly, these calculations also show that these central acceptor orbitals are lower in energy than the phen-like optical orbitals but are between those found in tatppβ and those for dppz, suggesting that the multielectron reduction properties may be retained even though the reduction potentials are significantly more negative.

The absorption spectra for the two complexes are similar but not identical. Both show strong, broad MLCT absorptions in the 440−480 nm region, which is typical for ruthenium(II) polypyridyl complexes. The lowest-energy LC transition at 444 nm in $\mathbf{2}^{4+}$ is coincident with the MLCT band, and the resulting spectra are a simple summation of the two components. In $\mathbf{1}^{4+}$, this transition is blue-shifted to 352 nm, which corresponds to an increase in energy of 0.69 eV, which closely matches the calculated increase in the LUMO energy of 0.64 eV. The low-energy LC band in $\mathbf{2}^{4+}$ reflects the lower energy of the LUMO in the tatppβ ligand, which is also manifested in the lower reduction potential associated with the first electroreduction peak in $\mathbf{2}^{4+}$ versus $\mathbf{1}^{4+}$ (Table 1).

It is clear that $\mathbf{1}^{4+}$ is photochemically reduced by one and then two electrons when irradiated with visible light in the presence of sacrificial donors. The singly reduced complex, formulated as $[(phen)_2Ru(tatppα^{\bullet-})Ru(phen)_2]^{3+}$ ($\mathbf{1}^{\bullet 3+}$), is characterized by a very broad, low-energy absorption centered at 890 nm, which is also seen in the cobaltocene-generated spectrum for $\mathbf{1}^{\bullet 3+}$. Although the complex is in acetonitrile, the decomposition of the TEA radical cation generates H^+ in solution, so it is possible to protonate the radical anion tatppα$^{\bullet-}$ to form H$\mathbf{1}^{4+}$. This seems unlikely by comparison with $\mathbf{2}^{\bullet 3+}$, which also shows a low-energy absorption at 975 nm for the tatpp$\beta^{\bullet-}$ radical anion. Chemical protonation of the singly reduced $\mathbf{2}^{\bullet 3+}$ results in rapid disproportionation, and bleaching of this near-IR band and similar behavior would be expected for $\mathbf{1}^{3+}$.

The second photoreduction of $\mathbf{1}^{\bullet 3+}$ to $\mathbf{1}^{2+}$ occurs much more slowly; however, the final product is clearly identical with the species generated by the reduction of $\mathbf{1}^{4+}$ with 2 equiv or more of cobaltocene.

Analysis of the spectroelectrochemical differential reflectance data indicates that the reduction process in $\mathbf{1}^{4+}$ is not as straightforward as it is in $\mathbf{2}^{4+}$ and that radical-anion dimerization is occurring. As is shown in Figures 7 and 8, $\mathbf{1}^{4+}$ is observed to undergo two sequential quasi-reversible reductive processes at low scan rates and low modulation frequencies. The first reduction wave of $\mathbf{1}^{4+}$ (peak C_I in the ac voltammogram; Figure 7c) is dynamically tracked by $\delta R/R$ at 850 and 460 nm (Figures 7a,b and 8a). The second reduction wave of $\mathbf{1}^{4+}$ (peak C_{II} in the ac voltammogram; Figure 8b) is clearly followed by $\delta R/R$ at 650 nm (Figure 8a, top). The back (anodic) scan shows a pattern similar to that of the reductive scan.

Both $\delta R/R$ potential profiles at 460 and 850 nm show a peak coincident with the ac voltammogram for the first electron uptake (Figure 7). After the reductive peak is passed in the voltammogram, the signal at 850 nm is seen to decrease as expected (Figure 8a, bottom); however, the 460 nm signal only partially drops and then shows a new broad peak, which gradually disappears as the potential reaches −1.20 V (Figure 8a, center). The increase of the 850 nm signal at potentials near −1.3 V is an artifact because subsequent reduction leads to a broad peak at 690 nm, which tails into the 850 nm region.

dx.doi.org/10.1021/ic2006698 |Inorg. Chem. 2011, 50, 9318–9328

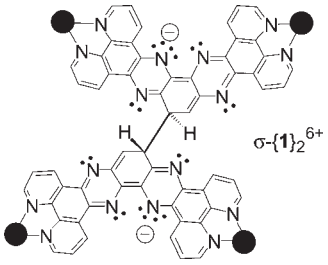

Figure 11. Structure of the σ-$\{\mathbf{1}\}_2^{6+}$ head-to-head dimer [solid black circles represent $Ru(phen)_2^{2+}$ fragments].

We propose the following mechanistic steps based on $\delta R/R$ profiles as a function of potential, the slowness of the second chemical reduction or second photochemical process, and the relative inertness of the final "doubly reduced" product toward reoxidation by O_2. Reduction, shown in reaction (2), is followed by dimerization of the tatppα radicals [reaction (3)] in an **EC**-type mechanism. The key chemical reaction step is the dimerization of two $\mathbf{1}^{\bullet 3+}$ radicals to form a σ-bond-bridged intermediate, σ-$\{\mathbf{1}\}_2^{6+}$, in agreement with the dimerization of aromatic anion and cation radicals.[50] We speculate that the "bent" structure of the tatppα ligand allows dimer formation in a head-to-head fashion, shown in Figure 11, which apparently is not sterically possible with the linear tatppβ ligand in $\mathbf{2}^{\bullet 3+}$.

$$\mathbf{1}^{4+} + e^- \rightleftarrows \mathbf{1}^{\bullet 3+} \quad \mathbf{E} \tag{2}$$

$$2\mathbf{1}^{\bullet 3+} \rightleftarrows \sigma\text{-}\{\mathbf{1}\}_2^{6+} \quad \mathbf{C} \tag{3}$$

The dimer formation [**C**, reaction (3)] trails the first electroreduction [**E**, reaction (2)] and is responsible for the second peak observed at 460 nm. The following electroreduction process (C_{II}/A_{II}) is associated with only an **E** mechanism [reaction (4)] involving one electron per complex or two electrons per dimer.

$$\sigma\text{-}\{\mathbf{1}\}_2^{6+} + 2e^- \rightleftarrows \sigma\text{-}\{\mathbf{1}\}_2^{4+} \quad \mathbf{E} \tag{4}$$

Thus, reaction (4) depicts the two-electron reduction of the new dimer σ-$\{\mathbf{1}\}_2^{6+}$ in which each tatppα ligand is effectively reduced by one electron to yield σ-$\{\mathbf{1}\}_2^{4+}$. This process appears as a single peak in the ac voltammogram and is accompanied by the appearance of a sharp $\delta R/R$ peak at 690 nm (followed at 650 nm in Figure 8).

This analysis indicates that the radical anion in the bent tatppα is more chemically reactive than the related radical anion in tatppβ. In fact, it is becoming clear that most laminate acceptor ligands are far more susceptible to dimerization, oxygen addition, or decomposition than tatppβ or tatpq upon reduction. In a previous effort to raise the energy of the LUMO on a tatppβ-type ligand, we added pendant methoxy groups off the central benzene ring and found that this complex photoeliminates methoxy or methyl groups.[51] Replacement of tatppβ with benzodipyrido[3,2-*a*:2′3′-*c*]phenazine leads to a mononuclear ruthenium(II) complex, which is converted to the quinone upon photoreduction and air exposure.[52] Even tatppβ can be involved in dimerization reactions, if only one end is coordinated to a $Ru(L{-}L)_2^{2+}$ fragment, because we have observed the reversible dimerization of the mononuclear complex $[(bpy)_2Ru(tatpp\beta)]^{2+}$ upon reduction to the radical anion.[53] We presume the most likely reason for the "inertness" of tatppβ in $\mathbf{2}^{4+}$ is due to steric bulk and have noted that, upon repeated reduction/air oxidation, even this complex slowly shows the appearance of the oxygenated quinone byproduct $\mathbf{3}^{4+}$.[26]

The extremely slow process of reoxidation of the doubly reduced product formed by chemical or photochemical processes is supportive of the proposed dimeric structure σ-$\{\mathbf{1}\}_2^{4+}$ and, more importantly, severely limits the complexe's usefulness for driving multielectron reactions. The electrochemical reversibility suggests that dimerization is a slow process that may be overcome or avoided given the proper ligand and complex design. If we are to develop photocatalysts capable of driving practical multielectron reactions, e.g., hydrogen evolution, these ligand-based side reactions must be mollified by appropriately building in steric bulk to prevent dimerization, working in oxygen-free environments to avoid oxygenation, and avoiding substituents that are good leaving groups. This is well within our means.

CONCLUSIONS

Both complexes $\mathbf{1}^{4+}$ and $\mathbf{2}^{4+}$ are competent for photodriven multielectron reduction and storage; however, each displays different strengths and weaknesses as functional photocatalysts. The complex with the linear tatppβ ligand, $\mathbf{2}^{4+}$, shows fast, facile, and reversible stepwise two-electron reduction by electrochemical or photochemical methods; however, the reduction potential of these stored electrons is modest, and most of the absorbed energy in a photochemical process is lost as heat. The complex incorporating the bent tatppα ligand can similarly undergo a photodriven two-electron reduction in a stepwise fashion, and it stores the electrons at potentials over 500 mV more negative than those in $\mathbf{2}^{4+}$. A simple calculation reveals that the photoreduced $\mathbf{1}^{2+}$ stores at least 90 kJ/mol more energy than $\mathbf{2}^{2+}$; however, the photoreduction process in $\mathbf{1}^{4+}$ is complicated by radical-anion dimerization side reactions that limit its utility in a photocatalytic role. We are attempting to build in steric bulk at the likely sites of dimerization to prevent this undesirable side reaction.

Importantly, we have demonstrated that it is possible to significantly raise the energy of the redox orbital in a laminate acceptor ligand relative to tatppα and still retain the multielectron-accepting function in a photochemical process. The excellent agreement between the observed redox properties and the orbital energies calculated by DFT theory for $\mathbf{1}^{4+}$ and $\mathbf{2}^{4+}$ suggests that computer modeling of the energetics and orbital electron distributions of potential laminate acceptor structures is a useful and efficient means of screening structures prior to synthesis in the laboratory. We are continuing to optimize the performance of this class of potential photocatalysts from the knowledge obtained thus far.

AUTHOR INFORMATION

Corresponding Author

*E-mail: rolezna@inifta.unlp.edu.ar (R.O.L.), macdonn@uta.edu (F.M.M.).

ACKNOWLEDGMENT

The authors thank Professor Peter Kroll and David Boston for assistance with the electronic structure calculations and Steven Poteet for repeating the synthesis of several compounds. We also thank the U.S. National Science Foundation [Grants CHE-0911720 (to F.M.M. and N.R.T.) and CHE-0840509 (500 MHz NMR)], the Robert A. Welch Foundation [Grant Y-1301

(to F.M.M.)], and BID 1728/OC-RA, PICT#26195/04 (to R.O.L.), for support of this research.

REFERENCES

(1) Meyer, T. J. *Acc. Chem. Res.* **1989**, *22*, 163–169.
(2) Amouyal, E. *Sol. Energy Mater. Sol. Cells* **1995**, *38*, 249–276.
(3) Campagna, S.; Puntoriero, F.; Nastasi, F.; Bergamini, G.; Balzani, V. *Top. Curr. Chem.* **2007**, *280*, 117–214.
(4) MacDonnell, F. M. In *Solar Hydrogen Generation: Toward a Renewable Energy Future*; Rajeshwar, K., Licht, S., Eds.; Springer Publishers: New York, 2008; Chapter 6.
(5) Watts, R. J. *Comm. Inorg. Chem.* **1991**, *11*, 303–337.
(6) Barton, C. E.; Lakkaraju, P. S.; Rampulla, D. M.; Morris, A. J.; Abelev, E.; Bocarsly, A. B. *J. Am. Chem. Soc.* **2010**, *132*, 11539–11551.
(7) Barber, J. *Curr. Opin. Struct. Biol.* **2002**, *12*, 523–530.
(8) Danks, S. M. *Photosynthetic Systems: Structure, Function, and Assembly*; Wiley: New York, 1983.
(9) Heyduk, A. F.; Nocera, D. G. *Science* **2001**, *293*, 1639–1641.
(10) Sutin, N.; Creutz, C.; Fujita, E. *Comm. Inorg. Chem.* **1997**, *19*, 67–92.
(11) Elvington, M.; Brown, J.; Arachchige, S. M.; Brewer, K. J. *J. Am. Chem. Soc.* **2007**, *129*, 10644–10645.
(12) Elvington, M.; Brewer, K. J. *Inorg. Chem.* **2006**, *45*, 5242–5244.
(13) Holder, A. A.; Swavey, S.; Brewer, K. J. *Inorg. Chem.* **2004**, *43*, 303–308.
(14) Esswein, A. J.; Veige, A. S.; Nocera, D. G. *J. Am. Chem. Soc.* **2005**, *127*, 16641–16651.
(15) Rosenthal, J.; Bachman, J.; Dempsey, J. L.; Esswein, A. J.; Gray, T. G.; Hodgkiss, J. M.; Manke, D. R.; Luckett, T. D.; Pistorio, B. J.; Veige, A. S.; Nocera, D. G. *Coord. Chem. Rev.* **2005**, *249*, 1316–1326.
(16) Pfennig, B. W.; Lockard, J. V.; Cohen, J. L.; Watson, D. F.; Ho, D. M.; Bocarsly, A. B. *Inorg. Chem.* **1999**, *38*, 2941–2946.
(17) Pfennig, B. W.; Mordas, C. J.; McCloskey, A.; Lockard, J. V.; Salmon, P. M.; Cohen, J. L.; Watson, D. F.; Bocarsly, A. B. *Inorg. Chem.* **2002**, *41*, 4389–4395.
(18) Molnar, S. M.; Nallas, G.; Bridgewater, J. S.; Brewer, K. J. *J. Am. Chem. Soc.* **1994**, *116*, 5206–5210.
(19) Hawecker, J.; Lehn, J.-M.; Ziessel, R. *New J. Chem.* **1983**, *7*, 271.
(20) Rau, S.; Schafer, B.; Gleich, D.; Anders, E.; Friedrich, M.; Gorls, H.; Henry, W.; Vos, J. G. *Angew. Chem., Int. Ed.* **2006**, *45*, 6215–6218.
(21) Ozawa, H.; Haga, M.-A.; Sakai, K. *J. Am. Chem. Soc.* **2006**, *128*, 4926–4927.
(22) Ozawa, H.; Yokoyama, Y.; Haga, M. A.; Sakai, K. *Dalton Trans.* **2007**, *12*, 1197–1206.
(23) Amouyal, E.; Keller, P.; Moradpour, A. *J. Chem. Soc., Chem. Commun.* **1980**, 1019–1020.
(24) Kirch, M.; Lehn, J.-M.; Sauvage, J.-P. *Helv. Chim. Acta* **1979**, *62*, 1345–1384.
(25) de Tacconi, N. R.; Lezna, R. O.; Konduri, R.; Ongeri, F.; Rajeshwar, K.; MacDonnell, F. M. *Chem.—Eur. J.* **2005**, *11*, 4327–4339.
(26) Konduri, R.; Ye, H.; MacDonnell, F. M.; Serroni, S.; Campagna, S.; Rajeshwar, K. *Angew. Chem., Int. Ed.* **2002**, *41*, 3185–3187.
(27) Lezna, R. O.; de Tacconi, N. R.; Macdonnell, F. M. *ECS Trans.* **2008**, *11*, 37–43.
(28) Chambron, J.-C.; Sauvage, J.-P.; Amouyal, E.; Kiffi, P. *Nouv. J. Chim.* **1985**, *9*, 527–529.
(29) Fees, J.; Kaim, W.; Moscherosch, M.; Matheis, W.; Klima, J.; Krejcik, M.; Zalis, S. *Inorg. Chem.* **1993**, *32*, 166–174.
(30) Turro, C.; Bossmann, S. H.; Jenkins, Y.; Barton, J. K.; Turro, N. J. *J. Am. Chem. Soc.* **1995**, *117*, 9026–9032.
(31) Amouyal, E.; Homsi, A.; Chambron, J.-C.; Sauvage, J.-P. *J. Chem. Soc., Dalton Trans.* **1990**, 1841–1845.
(32) Brennaman, M. K.; Alstrum-Acevedo, J. H.; Fleming, C. N.; Jang, P.; Meyer, T. J.; Papanikolas, J. M. *J. Am. Chem. Soc.* **2002**, *124*, 15094–15098.
(33) Paw, W.; Eisenburg, R. *Inorg. Chem.* **1997**, *36*, 2287–2293.
(34) Nakabayashi, K.; Kawano, M.; Yoshizawa, M.; Ohkoshi, S.; Fujita, M. *J. Am. Chem. Soc.* **2004**, *126*, 16694–16695.
(35) Kleineweischede, A.; Mattay, J. *Eur. J. Org. Chem.* **2006**, *4*, 947–957.
(36) Lezna, R. O.; de Tacconi, N. R.; Arvia, A. J. *J. Electroanal. Chem.* **1988**, *255*, 251–266.
(37) Brett, C. M. A.; Brett, A. M. O. *Electrochemistry: Principles, Methods, and Applications*; Oxford University Press: Oxford, U.K., 1993.
(38) Frisch, M. J.; Trucks, G. W.; Schlegel, H. B.; Scuseria, G. E.; Robb, M. A.; Cheeseman, J. R.; Montgomery, J. A., Jr.; Vreven, T.; Kudin, K. N.; Burant, J. C.; Millam, J. M.; Iyengar, S. S.; Tomasi, J.; Barone, V.; Mennucci, B.; Cossi, M.; Scalmani, G.; Rega, N.; Petersson, G. A.; Nakatsuji, H.; Hada, M.; Ehara, M.; Toyota, K.; Fukuda, R.; Hasegawa, J.; Ishida, M.; Nakajima, T.; Honda, Y.; Kitao, O.; Nakai, H.; Klene, M.; Li, X.; Knox, J. E.; Hratchian, H. P.; Cross, J. B.; Bakken, V.; Adamo, C.; Jaramillo, J.; Gomperts, R.; Stratmann, R. E.; Yazyev, O.; Austin, A. J.; Cammi, R.; Pomelli, C.; Ochterski, J. W.; Ayala, P. Y.; Morokuma, K.; Voth, G. A.; Salvador, P.; Dannenberg, J. J.; Zakrzewski, V. G.; Dapprich, S.; Daniels, A. D.; Strain, M. C.; Farkas, O.; Malick, D. K.; Rabuck, A. D.; Raghavachari, K.; Foresman, J. B.; Ortiz, J. V.; Cui, Q.; Baboul, A. G.; Clifford, S.; Cioslowski, J.; Stefanov, B. B.; Liu, G.; Liashenko, A.; Piskorz, P.; Komaromi, I.; Martin, R. L.; Fox, D. J.; Keith, T.; Al-Laham, M. A.; Peng, C. Y.; Nanayakkara, A.; Challacombe, M.; Gill, P. M. W.; Johnson, B.; Chen, W.; Wong, M. W.; Gonzalez, C.; Pople, J. A. *Gaussian03*; Gaussian, Inc.: Wallingford, CT, 2004.
(39) Kleineweischede, A.; Mattay, J. *Eur. J. Org. Chem.* **2006**, 947–957.
(40) Pietra, S.; Casiraghi, G. *Gazz. Chim. Ital.* **1967**, *97*, 1826–1836.
(41) Kim, M.-J.; Konduri, R.; Ye, H.; MacDonnell, F. M.; Puntoriero, F.; Serroni, S.; Campagna, S.; Holder, T.; Kinsel, G.; Rajeshwar, K. *Inorg. Chem.* **2002**, *41*, 2471–2476.
(42) MacDonnell, F. M.; Kim, M.-J.; Bodige, S. *Coord. Chem. Rev.* **1999**, *185−186*, 535–549.
(43) MacDonnell, F. M.; Kim, M.-J.; Wouters, K. L.; Konduri, R. *Coord. Chem. Rev.* **2003**, *242*, 47–58.
(44) Khanova, L. A.; Topolev, V. V.; Krishtalik, L. I. *Chem. Phys.* **2006**, *326*, 33–42.
(45) Connelly, N. G.; Geiger, W. E. *Chem. Rev.* **1996**, *96*, 877–910.
(46) Konduri, R.; de Tacconi, N. R.; Rajeshwar, K.; MacDonnell, F. M. *J. Am. Chem. Soc.* **2004**, *126*, 11621–11629.
(47) Gafney, H. D.; Adamson, A. W. *J. Am. Chem. Soc.* **1972**, *94*, 8238–8239.
(48) Elliott, C. M.; Redepenning, J. G. *J. Electroanal. Chem.* **1986**, *197*, 219–232.
(49) Wilson, R. A.; Pinyayev, T. S.; Membreno, N.; Heineman, W. R. *Electroanalysis* **2010**, *22*, 2162–2166.
(50) Rapta, P.; Schulte, N.; Schlüter, A. D.; Dunsch, L. *Chem.—Eur. J.* **2006**, *12*, 3103–3113.
(51) Singh, S.; de Tacconi, N. R.; Boston, D.; MacDonnell, F. M. *Dalton Trans.* **2010**, *39*, 11180–11187.
(52) Rau, S.; Schwalbe, M.; Losse, S.; Goerls, H.; McAlister, C.; MacDonnell, F. M.; Vos, J. G. *Eur. J. Inorg. Chem.* **2008**, 1031–1034.
(53) de Tacconi, N. R.; Chitakunye, R.; Macdonnell, F. M.; Lezna, R. O. *J. Phys. Chem. A* **2008**, *112*, 497–507.